

1 **Modulation of magnetospheric substorm frequency:**  
2 **Dipole tilt and IMF  $B_y$  effects**

3 **A. Ohma<sup>1</sup>, J. P. Reistad<sup>1</sup>, S. M. Hatch<sup>1</sup>**

4 <sup>1</sup>Birkeland Centre for Space Science, University of Bergen, Bergen, Norway

5 **Key Points:**

- 6 • Substorms are more frequent when the dipole tilt angle and IMF  $B_y$  have oppo-  
7 site compared to equal sign  
8 • This is a magnetospheric response, and cannot be explained by magnetosphere-  
9 ionosphere coupling affecting detection of substorms at ground  
10 • Whether the combination of  $B_y$  and tilt angle affects the dayside reconnection rate  
11 or magnetotail processes is currently unresolved

12 Compiled on 2020/10/22 at 13:34:41

---

Corresponding author: A. Ohma, [anders.ohma@uib.no](mailto:anders.ohma@uib.no)

**Abstract**

Using five independent substorm onset lists, we show that substorms occur more frequently when the Interplanetary Magnetic Field (IMF)  $B_y$  component and the dipole tilt angle  $\Psi$  have different signs as opposed to when they have the same sign. These results confirm that for  $\Psi \neq 0$  the magnetosphere exhibits an explicit dependence on the polarity of  $B_y$ , as other recent studies have suggested, and imply variation in the dayside reconnection rate and/or the magnetotail response. On the other hand, we find no clear relationship between substorm intensity and this explicit  $B_y$  effect. We additionally observe more frequent onsets for positive  $B_y$  in an onset list based on identifying negative bays in the auroral electrojet, regardless of season. Taking into account all five onset lists, we conclude that this phenomenon is not real, but is rather a consequence of the particular substorm identification method, which is affected by local ionospheric conditions that depend on  $B_y$  and  $\Psi$ .

**Plain Language Summary**

The solar wind that the Sun continuously emits is a plasma with an embedded magnetic field. The direction in which this magnetic field points changes frequently, and is among the most important factors in controlling geomagnetic activity, or how frequent and how bright the aurorae are. From the perspective of an observer at the magnetic pole in the Northern Hemisphere, a downward-pointing solar wind magnetic field yields the highest amount of geomagnetic activity and results in frequent and bright auroral displays. The magnetic field can also have a "sideways" component that points either toward dawn or toward dusk. It is often assumed that geomagnetic activity does not depend on whether the magnetic field points toward dawn or dusk. In this study, we show that around each solstice this sideways component does matter. When Earth is tilted towards the Sun (northern summer/southern winter), a dawnward-pointing magnetic field gives more frequent auroral breakups than the other. When Earth is tilted away from the Sun, a duskward-pointing magnetic field yields more auroral breakups. This insight improves our understanding of how Earth is coupled to space.

**1 Introduction**

A magnetospheric substorm is a process where magnetic flux and energy stored in the magnetotail lobes are unloaded by reconnection in the near-Earth tail, causing a global reconfiguration of the magnetosphere (Baker et al., 1996). The shape of the magnetotail changes from a stretched configuration to a more dipolar configuration during the unloading, and a field-aligned current system, known as the substorm current wedge, develops near midnight (McPherron et al., 1973; Kepko et al., 2015). The current wedge closes in the ionosphere, leading to an enhancement of the westward electrojet. This enhancement causes a pronounced negative bay in the northward component of magnetometers in the auroral zone, a signature that is directly linked to the auroral substorm, as first described by Akasofu (1964). The auroral substorm starts with an onset, which is a sudden, localized brightening of the aurora, typically located at the equatorial boundary of the discrete aurora. The intensified region then expands, both longitudinally and poleward; this period of the substorm is referred to as the expansion phase. The expansion phase is followed by a recovery phase, in which the magnetospheric system slowly reverts towards its pre-onset configuration.

Based on substorm onsets determined by electron injections at geosynchronous orbit, Borovsky et al. (1993) showed that substorms can occur periodically or randomly. They find that the most probable time between substorms is 2.75 h, which they interpret as the recurrence time between periodic substorms, while the mean wait time between randomly occurring substorms is approximately 5 h. Further, they suggest that the periodic substorms are associated with prolonged periods with favourable and quasi-

63 stable solar wind conditions, while the randomly occurring substorms reflect the random  
 64 variability of the solar wind. Since then, several studies have reported a quasi-periodic  
 65 occurrence of substorms, with a 2–4 hour recurrence time (e.g. Prichard et al., 1996; Huang  
 66 et al., 2003; Cai & Clauer, 2009; Hsu & McPherron, 2012). In an extensive study of sub-  
 67 storm occurrence frequency and recurrence times, Borovsky and Yakymenko (2017) iden-  
 68 tified onsets both from electron injections at geosynchronous orbit and by identifying jumps  
 69 in the *SML* index (Gjerloev, 2012). Both onset lists observe a most probable recurrence  
 70 time of  $\sim 3$  hours, and that this wait time is only weakly modulated by solar wind prop-  
 71 erties and the threshold used to identify onset. Further, they show that statistics of changes  
 72 in the orientation of the Interplanetary Magnetic Field (IMF) and intervals of above av-  
 73 erage solar wind forcing are consistent with the statistics of randomly occurring substorms.

74 However, there are also studies that report other time scales. Using the onset list  
 75 based on the *SML* index reported by Newell and Gjerloev (2011a), Newell and Gjerloev  
 76 (2011b) found that the intersubstorm wait time is best described by a broken power law,  
 77 and hence that the recurrence rate rises to their lowest time bin available (30 min), with  
 78 a mean of 4.4 h. Chu et al. (2015) used mid-latitude stations on the nightside to con-  
 79 struct an index of the power of magnetic perturbations in this region termed the Mid-  
 80 latitude Positive Bay (MPB) index, quantifying the intensity of the substorm current  
 81 wedge. Using this index to identify onsets, they found that the most probable time be-  
 82 tween onsets is 80 min, with median and mean recurrence time of  $\sim 3$  and  $\sim 8$  h, respec-  
 83 tively. Based on the same index, but using a different procedure to identify onsets, McPherron  
 84 and Chu (2018) found two peaks in the probability density function of the waiting times  
 85 between substorms, at 43 min and 152 min. While the latter peak is consistent with the  
 86  $\sim 3$ -hour recurrence time, the former peak suggest that also a shorter period could ex-  
 87 ist. The above illustrates that while the magnetospheric system does have inherent prop-  
 88 erties that affect the substorm occurrence frequency and recurrence times, the experi-  
 89 mental values of these parameters depend to some degree on which methodology for sub-  
 90 storm identification is employed.

91 Substorms are usually preceded by a growth phase (McPherron, 1970), a period  
 92 associated with intervals of enhanced solar wind forcing, typically associated with south-  
 93 ward IMF (Caan et al., 1977; Newell et al., 2013; Borovsky & Yakymenko, 2017). The  
 94 duration of this phase is typically 30–90 min (Li et al., 2013), during which magnetic flux  
 95 and energy is loaded to the magnetosphere. Caan et al. (1975, 1978) performed super-  
 96 posed epoch analysis of the lobe magnetic field, centered at substorm onset. Their anal-  
 97 ysis showed that the magnetic energy and flux increase in the hours leading up to on-  
 98 set, and rapidly decrease in the hour after onset, confirming that loading of the open mag-  
 99 netosphere occurs in the period before a substorm.

100 It is thus unsurprising that the occurrence frequency of substorms depends on the  
 101 upstream solar wind conditions. Kamide et al. (1977) showed that substorm activity be-  
 102 comes more frequent as the IMF becomes more southward. Substorms are also more fre-  
 103 quent in the declining phase of the solar cycle (Tanskanen, 2009; Borovsky & Yakymenko,  
 104 2017) and during coronal mass ejection and high-speed streams as opposed to during slow  
 105 solar wind conditions (Liou et al., 2018). Newell et al. (2013) demonstrated that the num-  
 106 ber of onsets per day correlates with a selection of solar wind coupling functions, but also  
 107 directly with the solar wind velocity. However, the relationship between this coupling  
 108 and the number of substorms is not necessarily linear, as the amount of flux closed by  
 109 a substorm can also depend on the preceding solar wind-magnetosphere coupling.

110 Solar wind coupling functions aim to quantify the rate at which energy or magnetic  
 111 flux is loaded into the magnetosphere through dayside reconnection. Over the last 50 years  
 112 a variety of such coupling functions have been derived either from theoretical consider-  
 113 ations or observations, or a combination of the two (e.g. Sonnerup, 1974; Burton et al.,  
 114 1975; Perreault & Akasofu, 1978; Vasyliunas et al., 1982; Newell et al., 2007; Milan et  
 115 al., 2012; Tenfjord & Østgaard, 2013; McPherron et al., 2015). The solar wind param-

eters used in these coupling functions are measured in Geocentric Magnetic (GSM) coordinates, in which the  $x$ -axis points toward the Sun and the  $y$ -axis is perpendicular to the Sun-Earth line and the magnetic dipole axis, positive towards dusk. The  $z$ -axis completes the right-handed system. A few commonly used functions are  $V_x B_s$  (Burton et al., 1975),  $V_x^{4/3} B_{yz}^{2/3} \sin^{8/3}(\theta_{CA}/2)$  (Newell et al., 2007) and  $\Lambda V_x^{4/3} B_{yz} \sin^{9/2}(\theta_{CA}/2)$  (Milan et al., 2012). Here,  $V_x$  is the  $x$  component of the solar wind velocity and  $B_{yz} = \sqrt{B_y^2 + B_z^2}$ , where  $B_y$  and  $B_z$  are the GSM components of the IMF.  $\theta_{CA}$  is the IMF clock angle defined as  $\arctan(B_y/B_z)$ , and  $B_s$  is equal to  $B_z$  when  $B_z < 0$  and zero when  $B_z > 0$ . The function estimated by Milan et al. (2012) also includes a scaling constant  $\Lambda = 3.3 \cdot 10^5 \text{ m}^{2/3} \text{ s}^{1/3}$ , making the unit of this function  $\text{V} = \text{Wb/s}$ , i.e. magnetic flux transport. Unless explicitly stated otherwise, IMF  $B_y$  (hereafter  $B_y$ ) and  $\theta_{CA}$  are calculated in GSM coordinates throughout this manuscript.

A common feature of the solar wind coupling functions is that they are symmetric with regard to the sign of  $B_y$ . Hence, it is presumed that only the magnitude of  $B_y$  plays a role in the dayside coupling. It has recently been documented, however, that certain aspects of the solar wind-magnetosphere-ionosphere coupling exhibit so-called explicit  $B_y$  effects. Although first pointed out by Friis-Christensen and Wilhjelm (1975), Holappa and Mursula (2018) further demonstrated and quantified the influence on the westward electrojet by the sign of  $B_y$ . They found that during local winter in the northern hemisphere, the  $AL$  index was  $\sim 50\%$  greater for positive  $B_y$  compared to negative  $B_y$ , during otherwise similar conditions. The opposite trend was observed during local summer, where the  $AL$  index was  $\sim 20\%$  greater for negative  $B_y$ . Consistent results were found using the  $K$  index of the Syowa station in the southern hemisphere, which is greater for positive  $B_y$  during local summer (northern winter) and greater for negative  $B_y$  during local winter (northern summer). The difference is also largest in the southern hemisphere during local winter. Similar seasonal differences in the  $AL$  index were shown by Laundal et al. (2016) and Friis-Christensen et al. (2017), and have also been reported in Birkeland currents derived from the Average Magnetic field and Polar current Systems (AMPS) model (Laundal et al., 2018). Based on measurements from the dark hemisphere, Friis-Christensen et al. (2017) suggested that the strength of the westward electrojet in the substorm current wedge was modulated by  $B_y$ , appearing larger in the northern hemisphere for positive  $B_y$  and in the southern hemisphere for negative  $B_y$ .

In lieu of a satisfying explanation of the dependence of ionospheric currents on the polarity of  $B_y$ , further studies have revealed other aspects of the coupled solar wind-magnetosphere-ionosphere system that exhibit similar dependence on  $B_y$  polarity. Reistad et al. (2020) found that the average size of the Region 1/Region 2 (R1/R2) current system, approximated as the radius of a circle fitted to Active Magnetospheric and Planetary Electrodynamics Response Experiment (AMPERE) observations, was significantly different under positive and negative  $B_y$ . This difference was only evident when the Earth's dipole tilt angle  $\Psi$  (i.e., degree of tilt of the Earth's dipole axis along the Sun-Earth line) was large. By convention,  $\Psi < 0$  corresponds to December solstice (northern winter/southern summer). Specifically, they found that for large, negative  $\Psi$ , positive  $B_y$  results on average in a slightly larger radius than negative  $B_y$  during otherwise similar conditions, as parameterized by a solar wind-magnetosphere coupling function (Milan et al., 2012). On the other hand, for large, positive  $\Psi$  (i.e., near June solstice) the radius of the R1/R2 current system has an opposite dependence on the sign of  $B_y$ . The same results were obtained from independent data in both hemispheres, which strongly suggests that this is not an effect of different magnetosphere-ionosphere (M-I) coupling in the two hemispheres, but is rather an effect of solar wind-magnetosphere interactions.

Holappa et al. (2020) recently reported a similar  $B_y$  polarity effect in the fluxes of high energy electron precipitation ( $> 30 \text{ keV}$ ) in the auroral region, most notably in the midnight to morning local time sector. They found significantly larger fluxes during the same conditions for which Reistad et al. (2020) find a larger radius of the R1/R2 cur-

169 rent system. Furthermore, their results are consistently seen in both hemispheres. Again,  
 170 this strongly suggests that the cause of their observed asymmetry is not an effect of the  
 171 different M-I coupling in the two hemispheres, but rather linked to a property of the solar  
 172 wind-magnetosphere interactions during intervals of significant  $B_y$  and  $\Psi$ .

173 Liou et al. (2020) investigated substorm occurrence rates with special emphasis on  
 174 the sign of  $B_y$ , also taking into account the level of upstream forcing. Their analysis indicated  
 175 a trend of  $\sim 30\%$  more substorms during positive compared to negative  $B_y$ . However,  
 176 Liou et al. (2020) only considered substorm lists based on detecting negative bays  
 177 in the *SML* index (Newell & Gjerloev, 2011a), and did not sort their analysis with respect  
 178 to dipole tilt or any other seasonal parameter. Here we demonstrate that both the  
 179 underlying substorm signature used to identify onsets and seasonal parameters may influence  
 180 the conclusions drawn from the analysis of substorm occurrence rates.

181 This paper presents analysis of substorm occurrence rates from five independent  
 182 lists of substorm onsets, all of which are sorted by IMF clock angle and dipole tilt angle.  
 183 These lists and our methodology for processing them are described in the following  
 184 section. We show the resulting onset frequency distributions in section 3. We discuss  
 185 the significance and physical implications of the results in section 4, and summarize  
 186 our findings in section 5.

## 187 2 Data processing

188 To determine how the substorm frequency depends on  $B_y$  and  $\Psi$ , we employ five  
 189 substorm onset lists, each based on different onset signatures from independent data sets.  
 190 Multiple lists are used to ensure that the observed trends are a signature of the magnetospheric  
 191 response, and not the result of M-I coupling or the local conditions in the hemisphere  
 192 where the observations are taken. The five substorm onset lists utilized in this  
 193 study are introduced below.

- 194 1. A distinct aspect of substorms is a negative bay in ground magnetometers at auroral  
 195 latitudes, caused by an enhancement of the westward electrojet. The *SML*  
 196 index (Newell & Gjerloev, 2011a) quantifies the strength of the westward electrojet,  
 197 and is based on  $\sim 100$  magnetometer stations at auroral latitudes in the northern  
 198 hemisphere from the SuperMAG network of ground observatories (Gjerloev,  
 199 2012). Using an algorithm to identify sharp and sustained drops in the *SML* index,  
 200 Newell and Gjerloev (2011a, 2011b), present an onset list (hereafter the N&G  
 201 list) that consists of 70,278 onsets identified during 1981–2019.
- 202 2. Positive bays in magnetometer data at mid-latitudes are a signature of field-aligned  
 203 currents associated with the substorm current wedge. A mid-latitude positive bay  
 204 (MPB) index using 41 ground magnetometers in both hemispheres (27 in the northern  
 205 hemisphere and 14 in the southern hemisphere) was put forward by Chu et  
 206 al. (2015); this index can be used to identify substorm onset by identifying bay  
 207 signatures (Chu et al., 2015; McPherron & Chu, 2018). We have used the onset  
 208 list described in McPherron and Chu (2018) (hereafter the McP&C list), which  
 209 consists of 57,558 onsets in the years 1982–2012 when their proposed threshold  
 210 value of the area of the positive bays,  $> 700 \text{ nT}^2 \cdot \text{min}$ , is used.
- 211 3. Another signature of substorm onset is Pi2 pulsations, which are oscillations in  
 212 the geomagnetic field observed at low- and mid-latitudes. A related index, termed  
 213 the Wave and planetary (Wp) index (World Data Center for Geomagnetism, Kyoto  
 214 & Nosé, 2016), was proposed by Nosé et al. (2012). This index is based on 1-s  
 215 magnetometer observations from 11 stations at low- and mid-latitudes in both  
 216 hemispheres (8 in the northern hemisphere and 3 in the southern hemisphere), and  
 217 is believed to reflect the wave power of the Pi2 pulsations. Nosé et al. (2012) also  
 218 proposed threshold criteria for identifying substorm onsets from the Wp index.

- 219 Using these criteria, we identify 14,075 onsets during 2005–2019 (hereafter the Nosé  
220 list).
- 221 4. Substorms are associated with a sudden, localized brightening of the aurora, which  
222 expands both longitudinally and poleward as the substorm progresses (Akasofu,  
223 1964). We have used a combination of two onset lists based on global far-ultraviolet  
224 images of the aurora made by the IMAGE mission (Frey et al., 2004; Frey & Mende,  
225 2006) and the Polar mission (Liou, 2010). These lists yield a combined total of  
226 6,727 identified substorm onsets during 1996–2007. We refer to this combined list  
227 as the F+L list. Note that each list is based on images from a single orbiting space-  
228 craft, which means that each spacecraft can only detect a substorm when it oc-  
229 curs within the field of view of the imaging instrument. Hence, this list does not  
230 provide full coverage of the given years. There are also three major data gaps in  
231 this dataset; during 3 Jul–3 Dec, 1996, during 6 Feb–15 May, 2000 and during 19  
232 Dec 2005–12 March 2007. These periods are discarded in the analysis. About 1/3  
233 of the IMAGE onsets and about 1/5 of the Polar onsets are from the southern hemi-  
234 sphere.
- 235 5. Yet another signature of substorm onset is the injection of energetic electrons into  
236 geosynchronous orbit (Kamide & McIlwain, 1974; Yeoman et al., 1994; Weygand  
237 et al., 2008), which leads to a sharp drop in the specific entropy of the hot elec-  
238 tron population (e.g. Borovsky & Cayton, 2011). Borovsky and Yakymenko (2017)  
239 present a substorm onset list (hereafter the B&Y list) based on identification of  
240 such drops using the Synchronous Orbit Particle Analyzer (SOPA) instrument on  
241 various geosynchronous spacecraft. The B&Y list is available at 30-min resolution,  
242 and gives 16,025 onsets in the years 1989–2007. Since the electron injection must  
243 drift to an orbiting spacecraft in order to be detected, the onsets determined by  
244 this method are systematically delayed by 0–30 min compared to the other lists.  
245 To account for this statistical bias, we have shifted the onsets in this list by  $-15$  min.

246 Before comparing substorm occurrence rates, we identify a potential source of bias  
247 in this analysis and describe how we account for it. Figure 1 displays the distribution  
248 of the clock angle  $\theta_{CA}$  during 1981–2019 in Geocentric Solar Magnetic (GSM) coordi-  
249 nates, Geocentric Solar Ecliptic (GSE) coordinates and Geocentric Solar Equatorial (GSEq)  
250 coordinates for  $\Psi < -15^\circ$  and  $\Psi > 15^\circ$  using a bin size of  $5^\circ$ . These  $\theta_{CA}$  values were  
251 calculated from the OMNI 1-min data, which is propagated to the nose of the Earth’s  
252 bow shock (King & Papitashvili, 2005). Rotation of the IMF vectors to GSEq coordi-  
253 nates were done with the aid of the International Radiation Belt Environment Model-  
254 ing (IRBEM) library (Boscher et al., 2004–2008) using SpacePy 0.2.1 (Morley et al., 2011).

255 While the two distributions are similar in GSEq coordinates, they are not similar  
256 in GSE and GSM coordinates; rather, they are rotated in opposite directions relative to  
257 the distributions in GSEq coordinates. For negative  $B_y$ , this apparent rotation corre-  
258 sponds to more southward and less northward IMF for positive tilt angles compared to  
259 negative tilt angles, and vice versa for positive  $B_y$ . This is the well known Russell-McPherron  
260 effect (Russell & McPherron, 1973), which describes how mapping from GSEq coordi-  
261 nates to GSM coordinates leads to seasonal biases in the clock angle distribution, and  
262 hence different levels of geomagnetic activity depending on the IMF sector polarity (to-  
263 ward/away). The effect maximizes around equinoxes, but is also substantial near sol-  
264 stices. While the effect near equinoxes is due to the large angle between Earth’s rota-  
265 tional axis and the normal of the ecliptic, the effect near solstice is due to the angle be-  
266 tween the ecliptic and the Sun’s equatorial plane.

267 Since the coupling between the IMF and terrestrial field is expected to be symmet-  
268 ric with regard to  $B_y$  and  $\theta_{CA}$  in GSM coordinates only, we need to account for these  
269 season-related biases in the IMF orientation rather than directly comparing the num-  
270 ber of substorm onsets for negative and positive  $B_y$ . We account for these biases as fol-  
271 lows. First, we divide the data into groups based on dipole tilt angle,  $\Psi$ , which was cal-

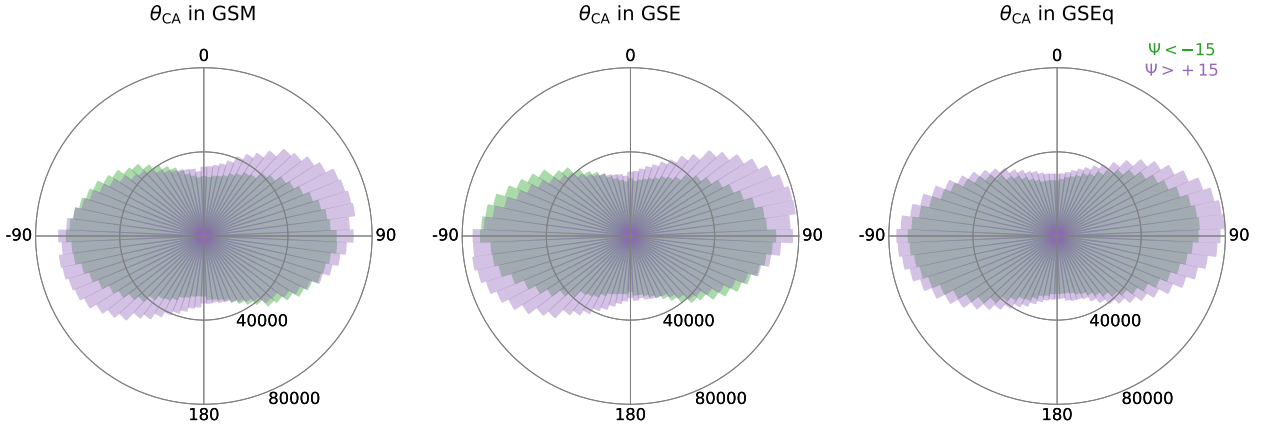


**Figure 1.** IMF clock angle distribution for  $\Psi < -15^\circ$  (green) and  $\Psi > 15^\circ$  (purple) in GSM (left), GSE (middle) and GSEq (right) coordinates.

272 culated using the method described in Laundal and Richmond (2017). We then bin the  
 273 onsets by the average clock angle in GSM coordinates in the hour before each onset, and  
 274 use the deciles of the absolute clock angle distribution during 1981–2019 to determine  
 275 the bin size; this yields 10 bins containing approximately the same number of hours of  
 276 data. We then normalize each clock angle bin by the number of days that the IMF clock  
 277 angle has that particular range of orientations over the duration of each specific substorm  
 278 list; thus each bin has units of substorm onsets per day. In order to estimate the uncer-  
 279 tainty of the obtained frequencies, we apply bootstrapping on the time series in each bin.  
 280 We draw 1000 random samples (with replacement) from the time series, where each new  
 281 sample has the same size as the original time series in that bin. From each sample we  
 282 calculate the number of onsets per day, and the standard deviation of all the estimated  
 283 onsets per day represents the standard error of the observed onset frequency.

### 284 3 Results

285 The distributions of substorm onsets per day are given in Figure 2. Each row cor-  
 286 responds to an independent substorm list, and each column corresponds to a different  
 287 tilt angle interval. Blue and orange indicate negative and positive  $B_y$ , respectively. The  
 288 numbers in the upper left corner of each panel are the total number of substorms for  $\pm B_y$   
 289 identified by the onset identification method associated with that list, and the ratio of  
 290 positive  $B_y$  to negative  $B_y$  onsets (black). The numbers in the lower right corner are the  
 291 average number of substorms per day found by averaging the distributions in each panel,  
 292 and the ratio of positive  $B_y$  to negative  $B_y$  onsets per day. These latter numbers are based  
 293 on the binned data, in which biases in the clock angle distribution are accounted for.

294 From the figure, it is immediately clear that the distributions for positive and nega-  
 295 tive  $B_y$  are different for large tilt angles. For  $\Psi < -15^\circ$ , there are more onsets per day  
 296 for positive  $B_y$  than for negative  $B_y$ . This is most clear in the N&G list (top row), but  
 297 consistently seen in all onset lists. The opposite effect is seen when  $\Psi > 15^\circ$ , where there  
 298 are more onsets per day for negative than positive  $B_y$ , again seen in all the list, albeit  
 299 less pronounced in the N&G and McP&C lists. The effect is most notable for  $45^\circ < |\theta_{CA}| <$   
 300  $135^\circ$ , which is when  $B_y$  dominates. That most of the asymmetry in onset frequency re-  
 301 mains after binning by clock angle (lower right in each panel), strongly suggests that non-  
 302 zero dipole tilt modulates the substorm frequency, in addition to any asymmetry caused  
 303 by the different clock angle distribution.

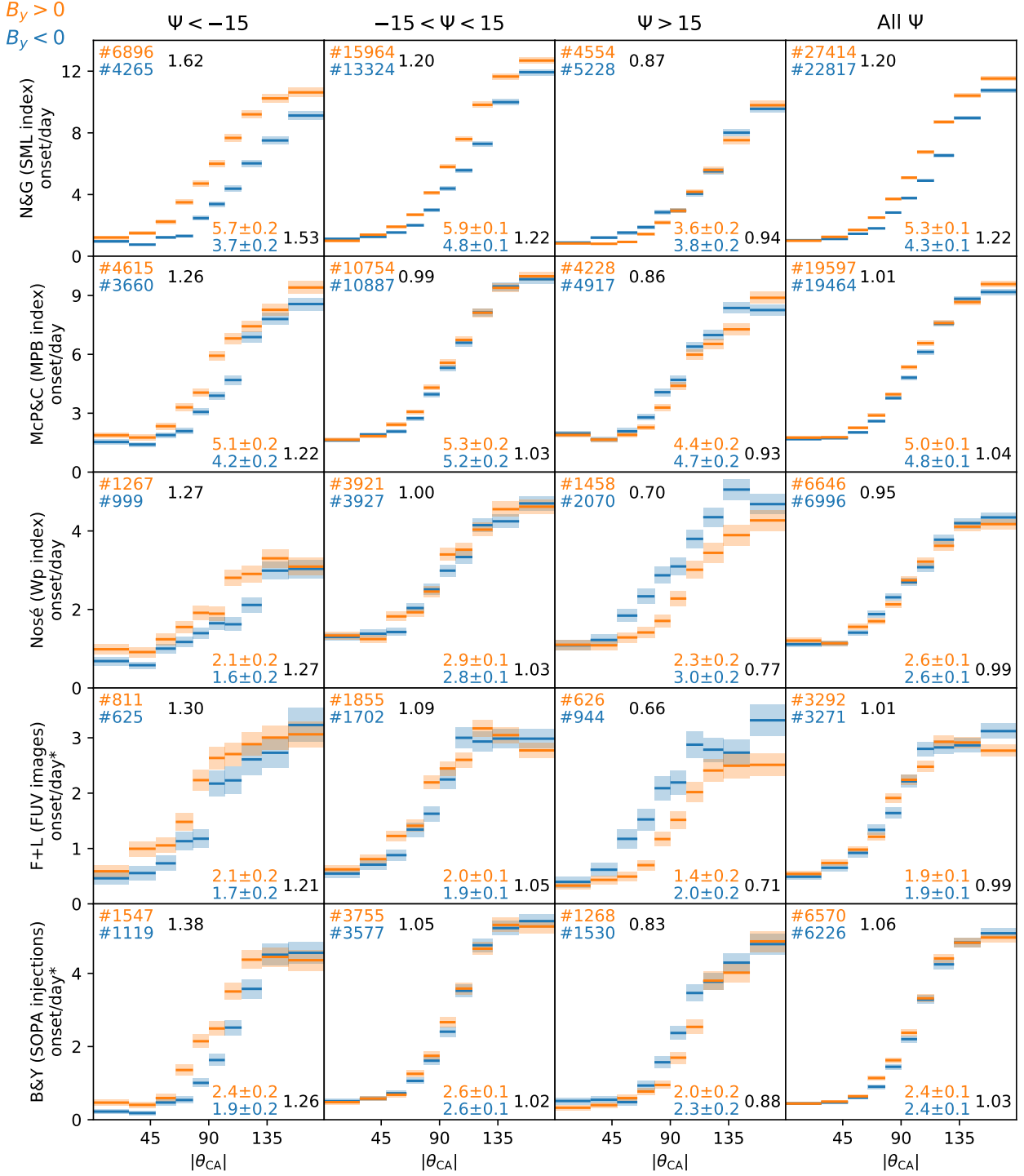


**Figure 2.** Onset occurrence rate for the five independent substorm onset lists. Blue colors indicate IMF  $B_y < 0$  and orange colors indicate IMF  $B_y > 0$ . The numbers in the upper left corner of each panel are the number of onsets for  $\pm B_y$ , and the fraction of positive to negative onsets. The shading above and below each line indicates the standard error of the onset occurrence rate, estimated via the bootstrapping procedure described in the main text. The numbers in the lower right corner of each panel are the average number of substorms per day for  $\pm B_y$ , and the fraction of positive to negative onsets per day. The '\*' symbol indicates lists based on spaceborne instruments, which do not have continuous coverage.

304 In the  $|\Psi| < 15^\circ$  tilt interval (second column) the distributions for  $\pm B_y$  are sim-  
 305 ilar and the average number of onsets per day about the same, with the notable excep-  
 306 tion of the N&G list, in which there are considerably more onsets for  $B_y > 0$ . In the  
 307 rightmost column of the figure we show the two distributions that result when no restric-  
 308 tion is placed on  $\Psi$ . These distributions are very similar to the  $|\Psi| < 15^\circ$  distributions,  
 309 with very similar distributions for  $\pm B_y$  for all lists except the N&G list.

310 Potential biases in the solar wind forcing could influence the distributions in Fig-  
 311 ure 2, although a large portion of any such bias is already accounted for by binning on  
 312 clock angle. Regardless, we have checked this by calculating the bin averages of the mean  
 313 solar wind forcing in the hour before onset (Figure A1 in Appendix A) and in the time  
 314 period covered by each onset list (Figure A2 in Appendix A). We find no systematic bi-  
 315 ases that can explain the differences in the onset distributions. The mean solar wind forc-  
 316 ing is typically a few percent larger for positive  $B_y$ , but this bias is consistent in all tilt  
 317 angle intervals. Newell et al. (2016) reported that the solar wind speed is the best pre-  
 318 dictor of substorm probability. To check for potential biases, we repeat the above using  
 319 only the solar wind speed (Figures A3 and A4 in Appendix A). Again, we observe no  
 320 underlying biases that could explain the onset distributions. However, the weak trend  
 321 of higher solar wind coupling and solar wind speed observed for positive  $B_y$  could be the  
 322 source of the slightly more pronounced trends seen for negative compared to positive  $\Psi$ ,  
 323 and the slightly higher onset rate for  $B_y > 0$  when  $|\Psi| < 15^\circ$ .

324 There appears to be a seasonal bias in the Nosé list, as the total number of sub-  
 325 storms are significantly lower for  $\Psi < -15^\circ$  compared to  $\Psi > 15^\circ$  (middle row in Fig-  
 326 ure 2. Such bias is not apparent in any of the other lists, which instead indicate that the  
 327 total number of onsets is about equal for large tilt angles. This bias could be a result  
 328 of the local season in which the observations are obtained, as only 3 of 11 observatories  
 329 are located in the southern hemisphere. However, the general trend for  $\pm B_y$  in the list  
 330 is in agreement with the observations from the other lists.

## 331 4 Discussion

332 The above analysis shows that the combination of dipole tilt and  $B_y$  modulate the  
 333 occurrence frequency of substorm onset. We will elaborate on the significance and phys-  
 334 ical implications of the result, and discuss important differences among the lists, in the  
 335 following sections.

### 336 4.1 An explicit $B_y$ dependence for large tilt angles

337 Despite being derived from independent data sources, the analysis of each of the  
 338 five substorm lists shown in Figure 2 shows the same general trend: More frequent sub-  
 339 storms when the sign of  $B_y$  and  $\Psi$  are opposite. The analysis thus reveals that the ori-  
 340 entation of the dipole axis, together with the orientation of  $B_y$ , plays an important role  
 341 in modulating the substorm onset frequency, which to our knowledge has not been shown  
 342 earlier. The results in Figure 2 seem to complement those of Holappa et al. (2020), who  
 343 found larger fluxes of high-energy electron precipitation in both hemispheres for oppo-  
 344 site compared to equal sign of  $B_y$  and  $\Psi$ . The increased substorm frequency for oppo-  
 345 site sign of the two parameters could explain the larger fluxes of high-energy electrons  
 346 observed in the ionosphere, as high-energy precipitation is known to be sensitive to in-  
 347 ner magnetospheric activations such as substorms (Beharrell et al., 2015). Hints of the  
 348 effect in Figure 2 can also be seen in Borovsky and Yakymenko (2017), although it was  
 349 not specifically called out by the authors. In their Table 2 and Figure 11 it can be seen  
 350 that the occurrence rate of substorms is greater in the away sector during winter and  
 351 greater in the toward sector during summer, both based on electron injections and *SML* jumps.

352 The higher occurrence frequency of substorms for opposite compared to equal signs  
 353 of  $B_y$  and  $\Psi$  can be interpreted in two ways: 1) Dayside opening of magnetic flux de-  
 354 pends on the combination of  $B_y$  and  $\Psi$ ; 2) The magnetotail responds differently to the  
 355 same loading of magnetic flux for the different combinations of  $B_y$  and  $\Psi$ . We elaborate  
 356 briefly on these two scenarios.

357 The shocked solar wind plasma, which interacts with the dayside magnetopause,  
 358 has different properties in the pre-noon and post-noon sectors due to the prevailing Parker  
 359 spiral structure of the IMF. As shown by, e.g., Walsh et al. (2014), the plasma  $\beta$  is typ-  
 360 ically larger in the pre-noon magnetosheath plasma. These dawn-dusk asymmetries in  
 361 the shocked solar wind plasma may affect the conditions for reconnection, which is thought  
 362 to be more effective in low- $\beta$  regions (Paschmann et al., 1986; Koga et al., 2019). The  
 363 quasi-parallel shock region (dawn) is also more prone than the quasi-perpendicular re-  
 364 gion (dusk) to the development of Kelvin-Helmholtz-Instabilities (KHI) (Nosé et al., 1995;  
 365 Dimmock et al., 2016; Nykyri et al., 2017). This leads to a dawn-favored plasma entry  
 366 into the magnetosphere through reconnection inside the KHI vortices.

367 However, a dawn-dusk asymmetry is alone insufficient to explain putative  $B_y$  po-  
 368 larity effects on dayside reconnection, since the reconnection geometry for positive and  
 369 negative  $B_y$  is symmetric if  $\Psi = 0^\circ$ , only mirrored across the  $Y_{\text{GSM}}$  axis. Therefore, al-  
 370 though the reconnection rates might be different between the pre-noon and post-noon  
 371 sectors, the rates within each sector remain the same for both polarities of  $B_y$  when  $\Psi =$   
 372  $0$ . Thus the total rate of flux opening is the same regardless of the polarity of  $B_y$ . This  
 373 is consistent with the four onset lists showing little or no  $B_y$  polarity effect for small  $\Psi$ .  
 374 This situation changes when  $\Psi$  is large. Under these conditions the two hemispheres are  
 375 not symmetrically exposed to the solar wind and IMF, and differences can arise.

376 It is unfortunately not possible at present to relate substorm strength and frequency  
 377 to changes in dayside reconnection rate. Not only is the fraction of flux closure through  
 378 substorms to the opening of flux on the dayside unknown, it may also depend on  $\Psi$  and  
 379  $B_y$ . Quantitative estimates of the degree of influence on the total dayside reconnection  
 380 rate, including all the relevant physics, remain a theoretical and observational challenge.

381 An alternative explanation is that the tail responds differently for opposite and equal  
 382 signs of  $B_y$  and  $\Psi$ . If we assume that the dayside reconnection rate is unaffected by the  
 383 sign of  $B_y$ , the same amount of flux is added to the magnetosphere for  $\pm B_y$ . This means  
 384 that the same amount of flux must, at some point, close again in the tail. Since the ob-  
 385 served substorm frequency does vary with  $B_y$  polarity and dipole tilt, this could either  
 386 mean that the average amount of flux closed by the substorms also differs (e.g., more  
 387 frequent and weaker substorms for  $B_y$  and  $\Psi$  with opposite signs, and less frequent and  
 388 stronger substorms for  $B_y$  and  $\Psi$  with the same sign), that substorms are more prone  
 389 to lead to steady magnetospheric convection (SMC) (c.f. Sergeev et al., 1996) for one  
 390 combination than the other, or that the flux throughput is accommodated without ini-  
 391 tiating substorms.

392 While we do not conjecture why the tail should respond differently, it is in any case  
 393 known that the geometry of the closed tail is influenced both by  $\Psi$  and  $B_y$ . It is pos-  
 394 sible that a combination of plasma sheet warping for  $\Psi \neq 0$  (Russell & Brody, 1967;  
 395 Fairfield, 1980; Tsyganenko & Fairfield, 2004) and plasma sheet rotation when  $B_y \neq 0$   
 396 (Cowley, 1981; Liou & Newell, 2010) causes different conditions for tail reconnection and  
 397 substorm activation in the pre-midnight sector, where substorms are preferably initiated  
 398 (Frey et al., 2004; Liou, 2010; Grocott et al., 2010). It has also been shown by Milan et  
 399 al. (2019) that high-latitude onsets are more prone to develop into SMC events, whereas  
 400 low-latitude onsets experience convection-breaking (Grocott et al., 2009) that leads to  
 401 loading-unloading cycles. Furthermore, the average size of the polar cap is expanded for  
 402 opposite compared to equal sign of  $B_y$  and  $\Psi$  (Reistad et al., 2020); this effect might also  
 403 influence the substorm occurrence rates.

404

## 4.2 Are substorms generally more frequent for positive $B_y$ ?

405

406

407

408

409

410

411

412

413

414

415

416

417

418

Recently, Liou et al. (2020) reported that substorms are generally more frequent (and stronger) for positive compared to negative  $B_y$ , regardless of season. Using the N&G onset list, which is based on identifying negative bays in the  $SML$  index, and taking into account the level of upstream solar wind forcing, they report that substorms are about 30% more common for positive compared to negative  $B_y$ . The same trend is found for in our analysis, as seen in the top row of Figure 2. Both for small tilt angles and when we do not impose a restriction on dipole tilt angle we observe 22% more onsets for  $B_y > 0$  compared to  $B_y < 0$ . Similar trends are also seen in other onset lists based on the  $SML$  index (Forsyth et al., 2015; Borovsky & Yakymenko, 2017, not shown). However, this trend is not observed for any of the other lists. It is therefore necessary to address why the onset distributions based on negative bays in the auroral electrojet in the northern hemisphere deviates from the distributions based on other onset signatures – are substorms in fact more common for positive compared to negative  $B_y$ , or is this trend related to some other physical conditions affecting the detection differently for  $\pm B_y$ ?

419

420

421

422

423

424

425

426

427

428

429

If global magnetospheric substorms are generally more frequent and stronger for positive  $B_y$ , the effect should be observed in both the northern and southern hemisphere. To address this point, we perform a superposed epoch analysis based on data from both hemispheres. For the northern hemisphere we use the standard  $SML$  index, which is based on magnetometers with magnetic latitude between  $40^\circ$  and  $80^\circ$ . For the southern hemisphere we have compiled a corresponding  $SML^*$  index, which is based on all available SuperMAG magnetometers with magnetic latitude between  $-40^\circ$  and  $-80^\circ$ . We strongly emphasize that the magnetometers in the southern hemisphere are few and unevenly distributed, and quantitative comparison to the northern hemisphere counterpart is probably not warranted. However, the analysis can yield a qualitative description of any differences in the response between the hemispheres.

430

431

432

433

434

435

436

437

Figure 3 displays the superposed epoch analysis of the  $SML$  index (top) and the  $SML^*$  index (bottom), centered at substorm onsets identified by McP&C, during 1994–2012. This analysis includes only substorm onsets for which the average clock angle in the hour before onset is in the interval  $45^\circ < |\theta_{CA}| < 135^\circ$ . Each column corresponds to a different dipole tilt interval. Blue and orange indicate negative and positive  $B_y$ , respectively, and the shaded area indicates the standard error of the mean. The numbers in the upper right corner indicate the drop for each curve. This value was determined by subtracting the minimum values from the maximum value near onset ( $\pm 5$  min).

438

439

440

441

442

443

444

445

446

447

448

449

450

451

452

For the  $SML$  index in the northern hemisphere, we observe an opposite trend for  $\pm B_y$  when  $\Psi$  is large; the average curve for positive  $B_y$  is below the average curve for negative  $B_y$  when  $\Psi < -15^\circ$ , and vice versa for  $\Psi > 15^\circ$ . The trend is more pronounced for  $\Psi < -15^\circ$ . For the  $SML^*$  index we observe the same trends; the average curve for positive  $B_y$  is below the average curve for negative  $B_y$  when  $\Psi < -15^\circ$ , and vice versa for  $\Psi > 15^\circ$ , also in the southern hemisphere. These observations are in agreement with the monthly averages of the  $AL$  index (northern hemisphere) and the  $K$  index of the Japanese Syowa station (southern hemisphere) presented by Holappa and Mursula (2018). This illustrates the global nature of the explicit  $B_y$  effect, yielding a stronger westward electrojet for opposite compared to equal sign of  $B_y$  and  $\Psi$  in both hemispheres. The perturbations in Figure 3 are much weaker in the southern hemisphere than in the northern hemisphere, but this is expected as the average distance from the substorm current system to the ground stations is much larger there. Despite this difference, the general trends observed are remarkably consistent between the hemispheres when the sign of  $B_y$  and  $\Psi$  is reversed.

453

454

455

For  $|\Psi| < 15^\circ$  and for all  $\Psi$  (second and rightmost columns), opposite trends are observed in the two hemispheres. The negative bays in the  $SML$  index are more pronounced for  $B_y > 0$ , with a sharper and deeper drop, in both subsets. This is consistent with

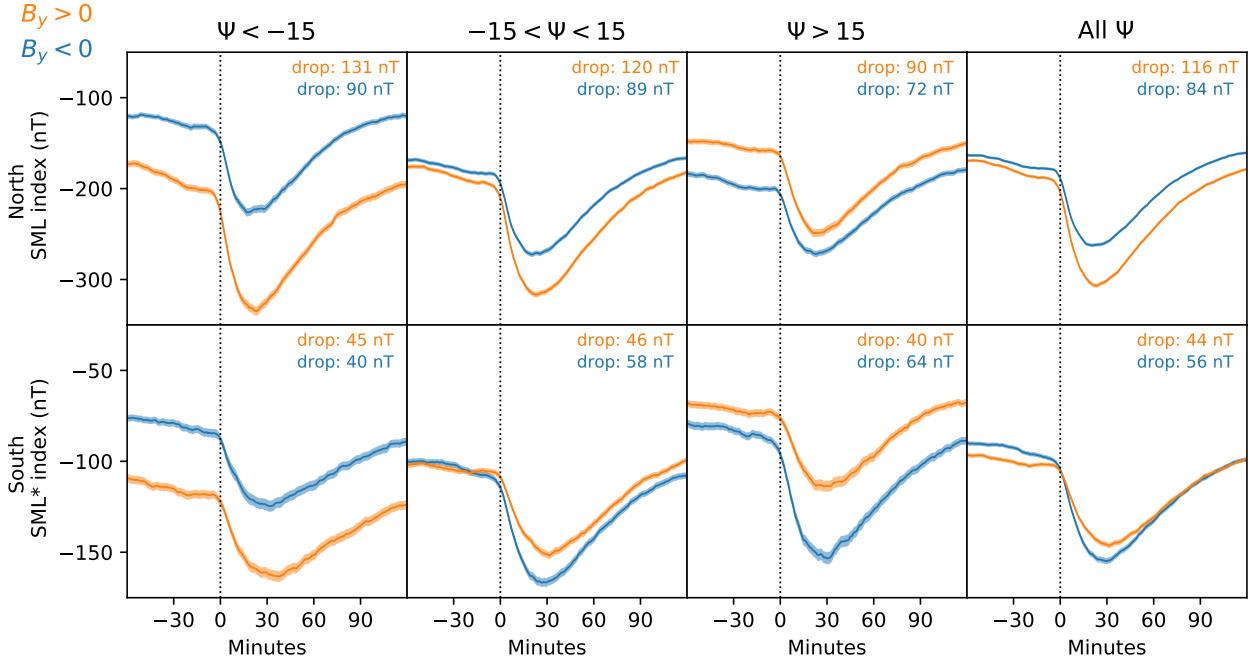


**Figure 3.** Superposed epoch analysis of the *SML* index based on magnetometers in the northern hemisphere (top) and a compiled *SML\** index based on magnetometers in the southern hemisphere (bottom) during 1994–2012. Zero epoch corresponds to substorm onset in the McP&C list. Blue and orange indicate negative and positive  $B_y$ , respectively. Only onsets for which the average clock angle in the hour before onset is in the interval  $45^\circ < |\theta_{CA}| < 135^\circ$  are included.

Liou et al. (2020), who find a general trend of more frequent and stronger substorms for positive  $B_y$ . However, the negative bays in the *SML\** index are more pronounced for negative  $B_y$  (larger drop). Since this particular response in Figure 3 is opposite in the southern and northern hemisphere, it cannot represent a global difference between positive and negative  $B_y$ . Rather, it indicates that the difference is due to conditions in the local hemisphere. We suggest that the geometry of high-latitude current systems causes these trends, which varies drastically with the sign of  $B_y$ . The geometry of the current systems is, however, expected to be approximately equal in the two hemispheres if the sign of  $B_y$  and  $\Psi$  is reversed. This is consistent with the trends in Figure 3.

Regardless of the exact source of the discrepancy between positive and negative  $B_y$ , the trends in Figure 3 illustrate how any algorithm designed to identify sharp and/or sustained drops in auroral electrojet-based indices from the northern hemisphere is more prone to detect onsets for  $B_y > 0$  compared to  $B_y < 0$ . If the spatial coverage of magnetometers in the southern hemisphere had allowed, these results suggest that the opposite would have been seen in an onset list based on southern hemispheric observations. Additionally, none of the other onsets lists observe a large general trend of higher onset frequency for the two  $B_y$  polarities, either during small dipole tilt conditions or when no restriction on the dipole tilt angle is imposed. These lists are also more robust with regards to local ionospheric conditions affecting the detection differently for  $\pm B_y$ , as they are either based on observations from both hemispheres (McP&C, Nosé and F+L) or obtained in the magnetosphere (B&Y). Hence, in contrast to (Liou et al., 2020), we conclude that there is no strong general trend toward more substorms when  $B_y$  is positive compared to negative, regardless of the dipole tilt orientation. If any such effect exists,

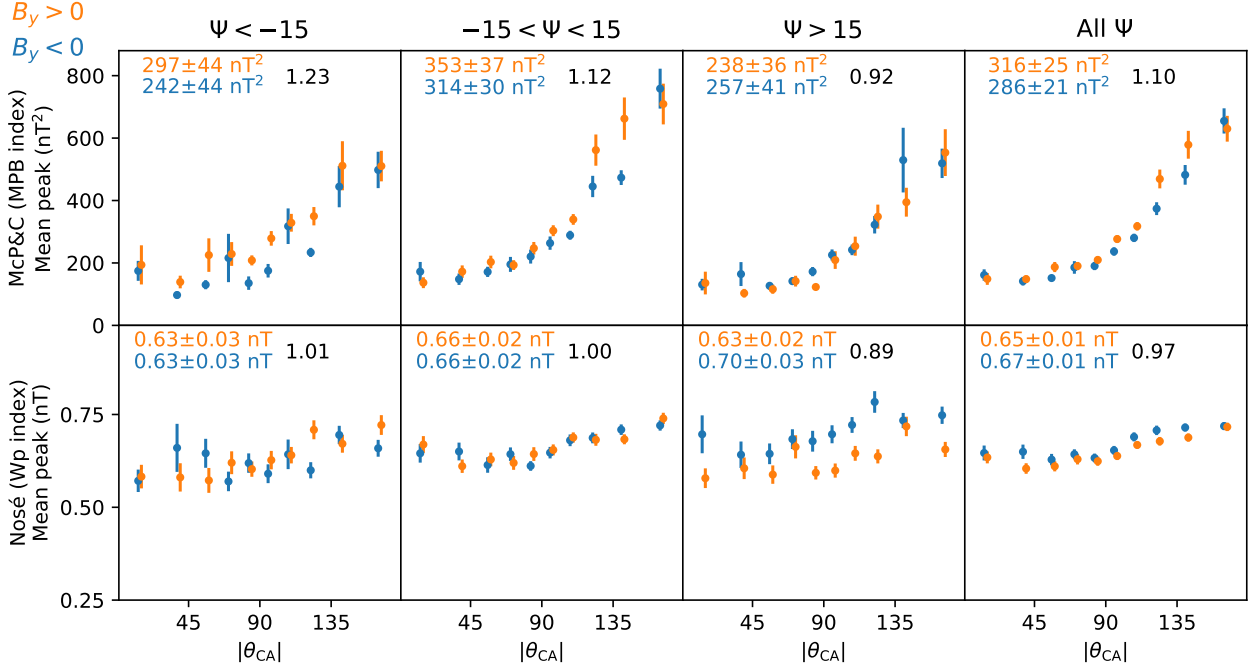


**Figure 4.** The mean peak value of the MBP index for the McP&C onsets (top) and the mean peak value of the Wp index for the Nosé onsets (bottom) in each clock angle bin used in Figure 2. Blue colors indicate  $B_y < 0$  and orange colors indicate  $B_y > 0$ . The error bars indicate the standard error of the mean in each bin and the numbers are the mean and error of the binned values in each panel for  $\pm B_y$ .

479 its influence on the daily rate of substorm occurrence is relatively minor, and no larger  
 480 than a few percent.

### 481 4.3 Do the combination of $B_y$ and dipole tilt affect substorm intensity?

482 It is relevant to address whether or not substorm intensity is affected by the sign  
 483 of  $B_y$  for large tilt angles. One option would have been to consider the magnitude of the  
 484 *SML* index, but as shown in the previous section, the difference between positive and neg-  
 485 ative  $B_y$  is considerably affected by local ionospheric conditions. The magnitude of the  
 486 *SML* index can therefore not be used to compare the intensity of substorms under dif-  
 487 ferent  $B_y$  conditions. Due to the few and unevenly distributed magnetometers in the south-  
 488 ern hemisphere, any quantitative comparison between the two hemispheres is difficult.  
 489 We have therefore considered two other alternatives.

490 The McP&C onset list provides several parameters describing each positive bay:  
 491 peak value, area and duration of each pulse, as quantified by the MPB index (Chu et  
 492 al., 2015). We have considered the peak values, which corresponds to the maximum power  
 493 of the magnetic perturbations at mid-latitudes caused by the substorm current wedge,  
 494 but similar trends are also seen for the Bay area and when we subtract the baseline value  
 495 of the MPB index based on the start and end values of each peak. The mean peak value  
 496 of all McP&C onsets within each bin used in Figure 2 is shown in the top row of Fig-  
 497 ure 4. We observe higher mean peaks for positive  $B_y$  when  $\Psi < -15$  and weak indi-  
 498 cations of higher peaks for negative  $B_y$  when  $\Psi > 15$ . There is also a weak trend of higher

499 mean peaks for  $|\Psi| < 15$ , and when we put no restriction on  $\Psi$ . However, neither trend  
500 is statistically significant.

501 The magnitude of the Wp index can be regarded as the average amplitude of night-  
502 side Pi2 pulsation (Nosé et al., 2012), which again correlates with auroral power (Takahashi  
503 et al., 2002; Takahashi & Liou, 2004). We have therefore found the maximum value of  
504 the Wp index in the 20 minutes following each Nosé onset. The mean of these peak val-  
505 ues are shown in the bottom row in Figure 4, again using the same bins as in Figure 2.  
506 While we observe no systematic or significant difference between positive and negative  
507  $B_y$  for  $\Psi < -15$  and  $|\Psi < 15|$ , the values are significantly larger for negative  $B_y$  when  
508  $\Psi > 15$ . The same is seen when we put no restriction on  $\Psi$ , but this is most likely just  
509 a reflection of the difference in substorm occurrence rate seen in Figure 2, leading to a  
510 bias towards positive tilt angles.

511 Based on the combined results in Figure 4, we see either no difference for  $\pm B_y$ , or  
512 a weak signature of higher substorm intensity for opposite compared to equal sign of  $B_y$ .  
513 Hence, there is no indication that substorms are stronger and less frequent for equal sign  
514 of  $B_y$  and  $\Psi$ . However, as the values reported here are proxies of the substorm inten-  
515 sity, and do not directly measure either dissipated energy or closure of magnetic flux,  
516 the evidence presented here is only suggestive.

## 517 5 Summary

518 Using five independent substorm onset lists, we have shown that the substorm fre-  
519 quency depends on the sign of IMF  $B_y$  when the Earth's dipole tilt angle is large. Specif-  
520 ically, we find a higher substorm frequency when  $B_y$  and  $\Psi$  have opposite compared to  
521 equal signs. Since substorms are a global, magnetospheric process, this confirms that substorm-  
522 related magnetospheric processes explicitly depend on the polarity of  $B_y$ . We have out-  
523 lined possible physical mechanisms, and pointed out the present lack of a coherent un-  
524 derstanding of these processes. This should encourage further research effort into deter-  
525 mining why some magnetospheric processes depend explicitly on the sign of  $B_y$ . When  
526 we consider substorm intensity, we find no clear relationship between substorm inten-  
527 sity and the sign of  $B_y$  and  $\Psi$ . Substorm intensity appears to be unchanged or only weakly  
528 enhanced for opposite sign of  $B_y$  and  $\Psi$ .

529 With the exception of one onset list that is based on identifying negative bays in  
530 the westward electrojet, we find little or no difference in the substorm frequency for  $\pm B_y$   
531 for small tilt angles or when we do not impose a restriction on dipole tilt angle. We there-  
532 fore conclude that the magnetosphere only exhibits the explicit  $B_y$  effect when the dipole  
533 tilt is large, and that the general trend of more frequent onsets for  $B_y > 0$  compared  
534 to  $B_y < 0$  observed in the N&G list is a result on the ionospheric conditions and not  
535 the magnetospheric response.

## 536 Appendix A Solar wind coupling and velocity

537 In this appendix we provide four figures that explore potential biases in the solar  
538 wind distribution, which could affect the substorm onset distributions reported in Fig-  
539 ure 2. Figures A1 and A2, which are in the same format as Figure 2, explore the role  
540 of solar wind forcing as estimated using the coupling function presented by Milan et al.  
541 (2012). This function is  $\Lambda V_x^{4/3} B_{yz} \sin^{9/2} \frac{1}{2} \theta_{CA}$ , where  $V_x$  is the solar wind velocity in the  
542  $x$ -direction,  $B_{yz}$  is the magnitude of the IMF in the  $yz$ -plane and  $\theta_{CA}$  is the clock an-  
543 gle, all in GSM coordinates.  $\Lambda$  is a constant with value  $3.3 \cdot 10^5 \text{ m}^{2/3} \text{ s}^{1/3}$ . In Figure A1,  
544 we estimate the average rate of flux opened by dayside reconnection in the hour before  
545 onset via this coupling function for each identified substorm. We then calculate the bin  
546 averages in the same bins used in Figure 2. Blue colors indicate  $B_y < 0$  and orange col-  
547 ors indicate  $B_y > 0$ , and the error bars display the standard error of the mean. The

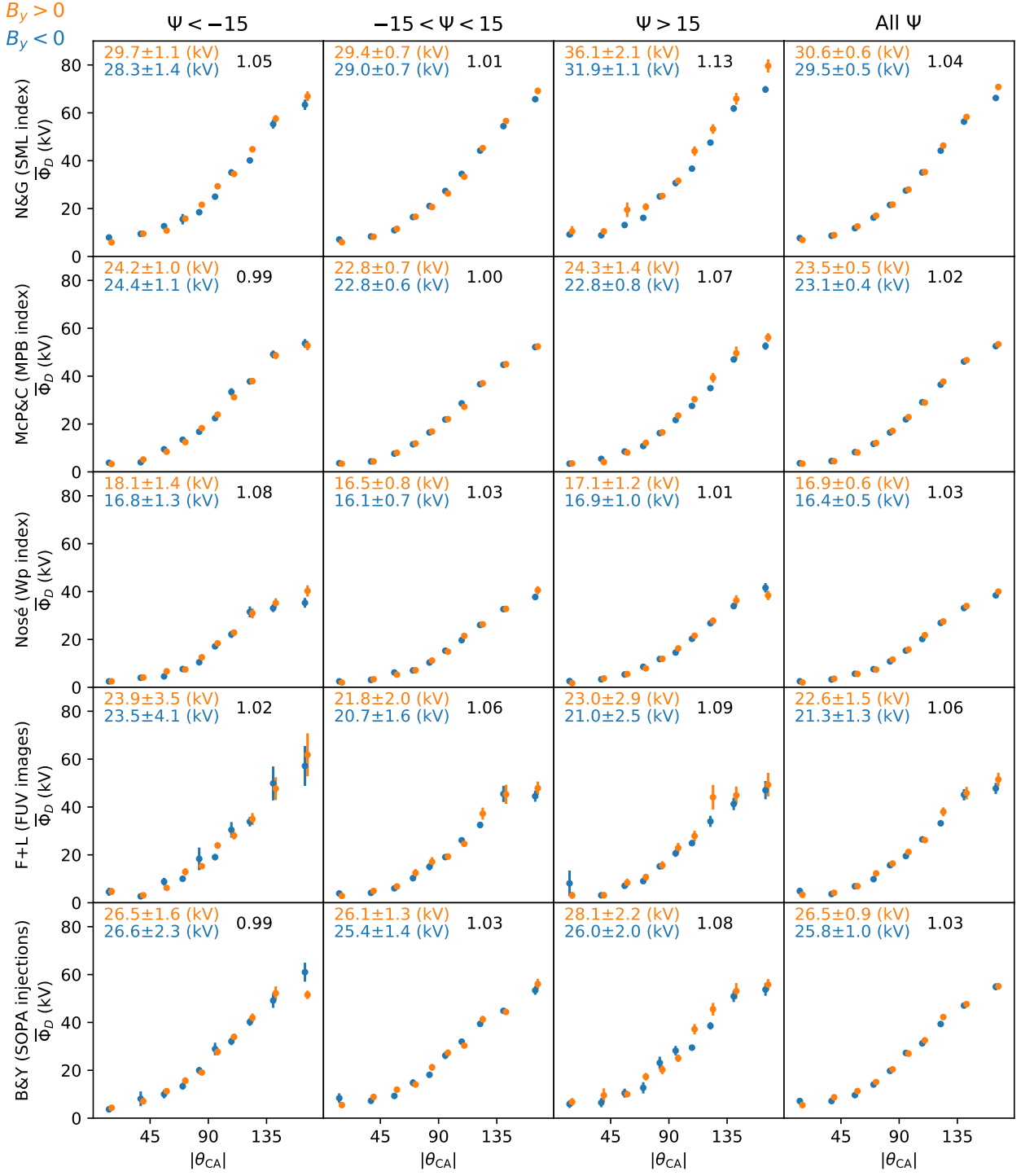


**Figure A1.** The mean solar wind forcing  $\bar{\Phi}_D$  in each clock angle bin used in Figure 2 based on the mean solar wind forcing in the hour before each onset. Blue colors indicate  $B_y < 0$  and orange colors indicate  $B_y > 0$ . The error bars indicate the standard error of the mean in each bin. The numbers are the mean and error of the binned values in each panel for  $\pm B_y$ , and the fraction of positive to negative solar wind forcing

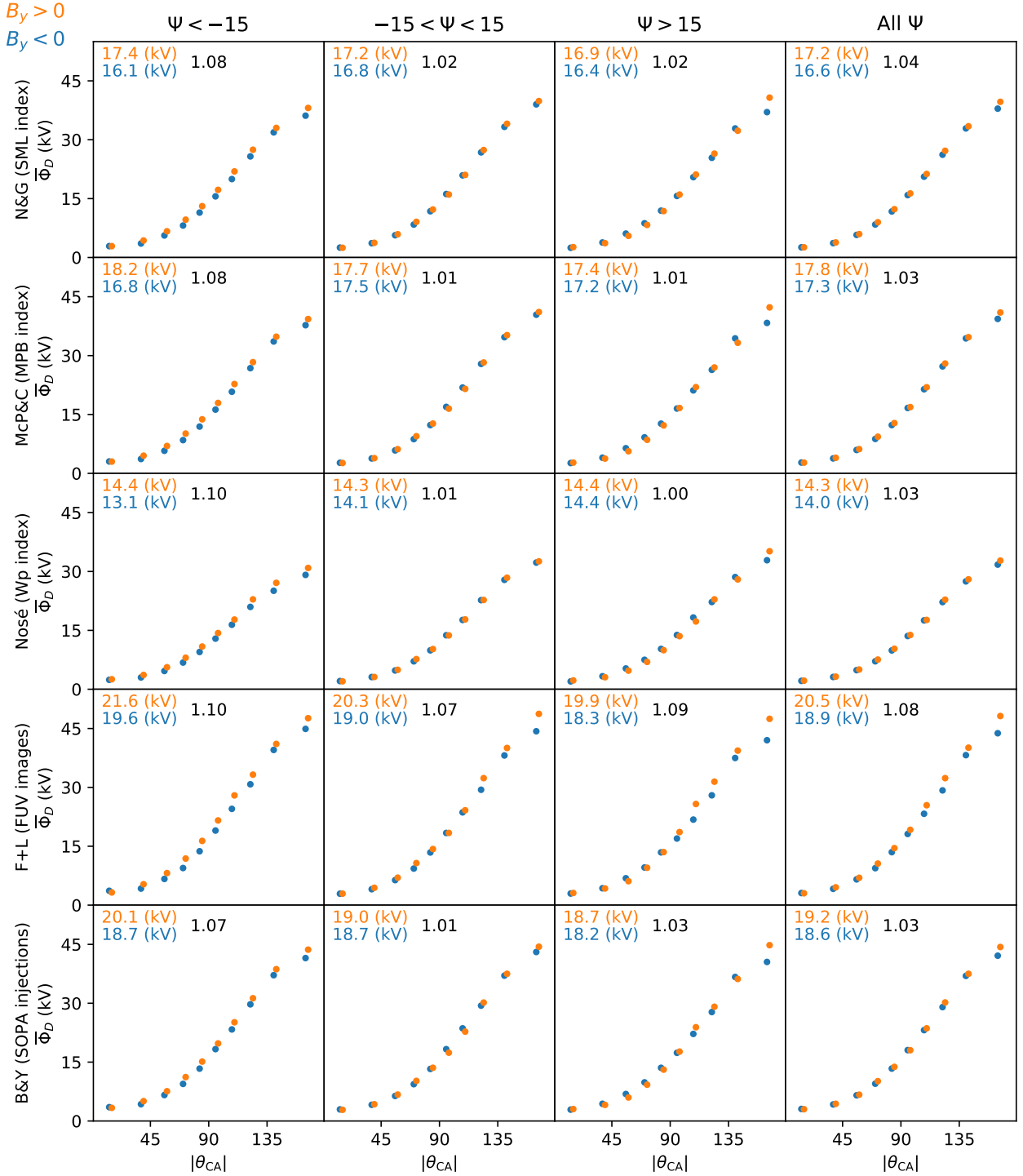


**Figure A2.** The mean solar wind forcing  $\bar{\Phi}_D$  in each clock angle bin used in Figure 2 for the entire duration of each substorm onset list. Blue colors indicate  $B_y < 0$  and orange colors indicate  $B_y > 0$ . The numbers are the mean of the binned values in each panel for  $\pm B_y$ , and the fraction of positive to negative solar wind forcing.

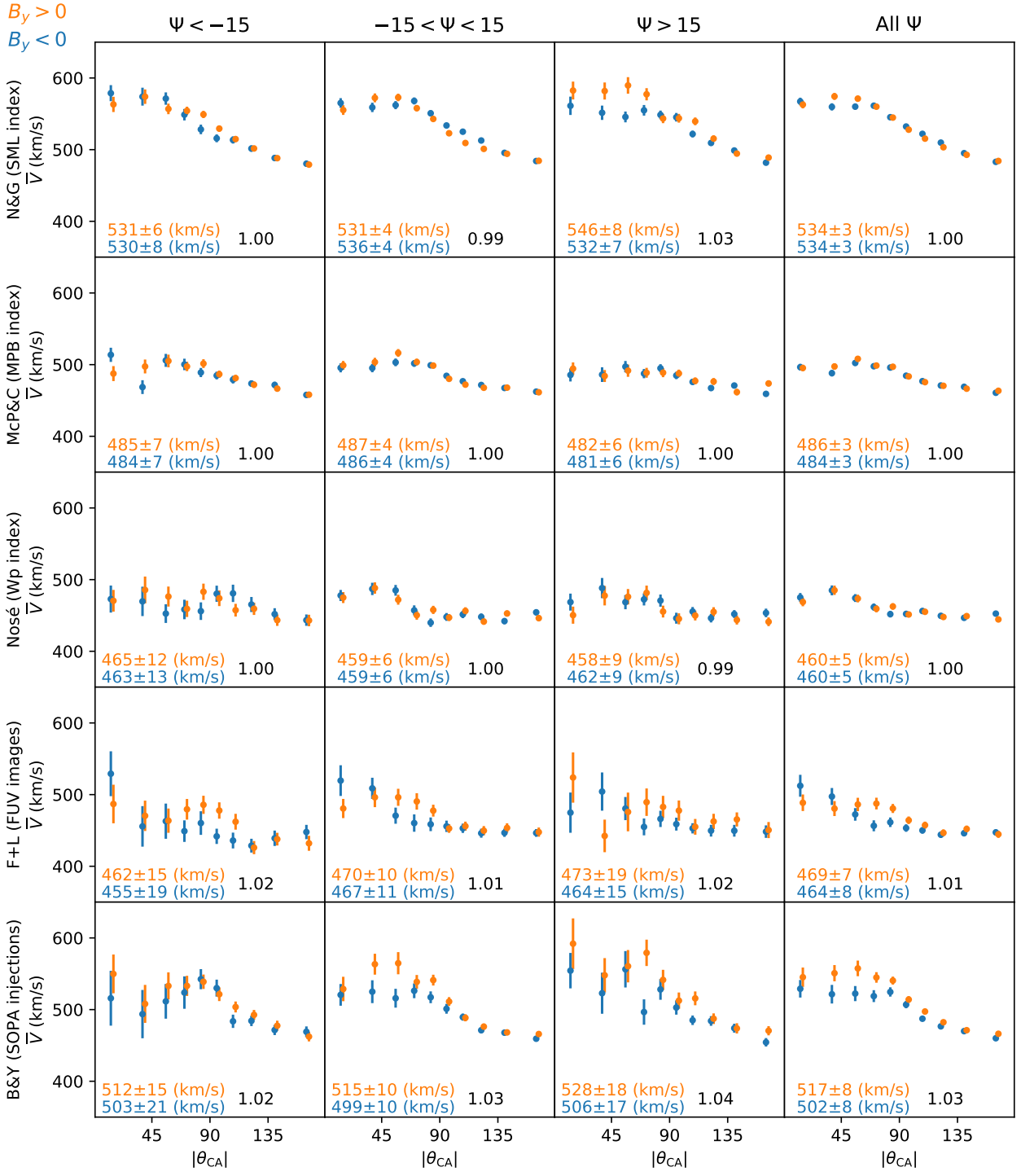


**Figure A3.** The mean solar wind speed  $\bar{V}_{SW}$  in each clock angle bin used in Figure 2 based on the mean solar wind speed in the hour before each onset. Blue colors indicate  $B_y < 0$  and orange colors indicate  $B_y > 0$ . The error bars indicate the standard error of the mean in each bin. The numbers are the mean and error of the binned values in each panel for  $\pm B_y$ , and the fraction of positive to negative velocities.

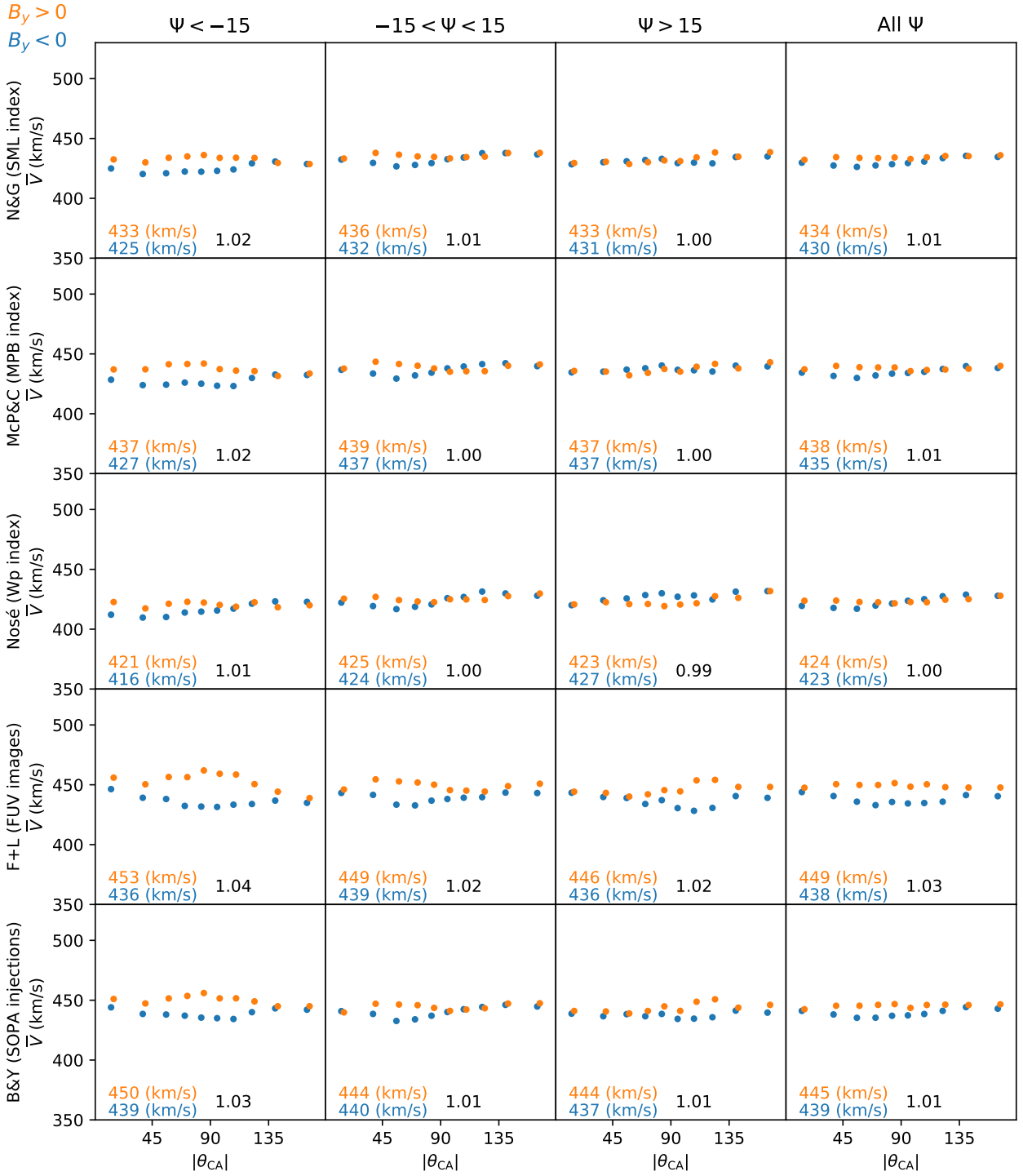


**Figure A4.** The mean solar wind speed  $\bar{V}_{\text{SW}}$  in each clock angle bin used in Figure 2 for the entire duration of each substorm onset list. Blue colors indicate  $B_y < 0$  and orange colors indicate  $B_y > 0$ . The numbers are the mean of the binned values in each panel for  $\pm B_y$ , and the fraction of positive to negative velocities

548 numbers in each panel indicate the average and error of the ten data points in each panel  
 549 for  $\pm B_y$ , and the fraction of positive to negative values. In Figure A2, we instead esti-  
 550 mate the bin averages based on all the 1-min OMNI data in the years spanned by each  
 551 onset list. Again, blue colors indicate  $B_y < 0$  and orange colors indicate  $B_y > 0$ , and  
 552 the numbers in each panel indicate the average of the ten data points in each panel for  
 553  $\pm B_y$ . Due to the large amount of data, statistical errors are negligible. Both figures show  
 554 that the solar wind coupling is about equal or a few percent larger for positive  $B_y$ , but  
 555 show no biases that could explain the observed onset trends in Figure 2.

556 Figure A3, which is in the same format as Figure A1, explores the role of the solar  
 557 wind speed before each identified onset. For each substorm, we estimate the mean  
 558 speed in the hour before substorm and then calculate the bin averages. The values are  
 559 very similar for  $\pm B_y$ , but slightly larger for  $B_y > 0$  in the B&Y list. Figure A4, which  
 560 is in the same format as Figure A2, explores potential biases in the solar wind speed in  
 561 the years spanned by each onset list. Here we see that the velocities are equal or a few  
 562 percent larger for positive compared to negative  $B_y$ .

### 563 Acknowledgments

564 This study was supported by the Research Council of Norway/CoE under contract 223252/F50.  
 565 The OMNI solar wind data was downloaded from [https://cdaweb.gsfc.nasa.gov/sp](https://cdaweb.gsfc.nasa.gov/sp_phys/data/omni/hro_1min/)  
 566 [\\_phys/data/omni/hro\\_1min/](https://cdaweb.gsfc.nasa.gov/sp_phys/data/omni/hro_1min/). We gratefully acknowledge the SuperMAG collaborators  
 567 (<http://supermag.jhuapl.edu/info/?page=acknowledgement>). The *SML* index, N&G  
 568 list and superMAG data were downloaded from <http://supermag.jhuapl.edu>. The McP&C  
 569 list was obtained from [https://agupubs.onlinelibrary.wiley.com/doi/full/10.1002/](https://agupubs.onlinelibrary.wiley.com/doi/full/10.1002/2017JA024766)  
 570 [2017JA024766](https://agupubs.onlinelibrary.wiley.com/doi/full/10.1002/2017JA024766). The Wp index, from which we derived the Nosé list, was downloaded from  
 571 <http://www.isee.nagoya-u.ac.jp/~nose.masahito/s-cubed/>. The B&Y list was ob-  
 572 tained from <https://agupubs.onlinelibrary.wiley.com/doi/abs/10.1002/2016JA023625>.  
 573 The IMAGE FUV onsets were obtained from <http://sprg.ssl.berkeley.edu/image/>  
 574 and the Polar UVI onsets from [https://agupubs.onlinelibrary.wiley.com/doi/full/](https://agupubs.onlinelibrary.wiley.com/doi/full/10.1029/2010JA015578)  
 575 [10.1029/2010JA015578](https://agupubs.onlinelibrary.wiley.com/doi/full/10.1029/2010JA015578). We thank K. M. Laundal for providing software to calculate  
 576 the dipole tilt angle (<https://github.com/klaundal/dipole>).

### 577 References

- 578 Akasofu, S.-I. (1964). The development of the auroral substorm. *Planetary and*  
 579 *Space Science*, *12*(4), 273 - 282. doi: [https://doi.org/10.1016/0032-0633\(64\)](https://doi.org/10.1016/0032-0633(64)90151-5)  
 580 [90151-5](https://doi.org/10.1016/0032-0633(64)90151-5)
- 581 Baker, D. N., Pulkkinen, T. I., Angelopoulos, V., Baumjohann, W., & McPherron,  
 582 R. L. (1996). Neutral line model of substorms: Past results and present view.  
 583 *Journal of Geophysical Research: Space Physics*, *101*(A6), 12975-13010. doi:  
 584 [10.1029/95JA03753](https://doi.org/10.1029/95JA03753)
- 585 Beharrell, M. J., Honary, F., Rodger, C. J., & Clilverd, M. A. (2015). Substorm-  
 586 induced energetic electron precipitation: Morphology and prediction. *Jour-*  
 587 *nal of Geophysical Research: Space Physics*, *120*(4), 2993-3008. doi:  
 588 [10.1002/2014JA020632](https://doi.org/10.1002/2014JA020632)
- 589 Borovsky, J. E., & Cayton, T. E. (2011). Entropy mapping of the outer elec-  
 590 tron radiation belt between the magnetotail and geosynchronous orbit.  
 591 *Journal of Geophysical Research: Space Physics*, *116*(A6), A06216. doi:  
 592 [10.1029/2011JA016470](https://doi.org/10.1029/2011JA016470)
- 593 Borovsky, J. E., Nemzek, R. J., & Belian, R. D. (1993). The occurrence rate of  
 594 magnetospheric-substorm onsets: Random and periodic substorms. *Jour-*  
 595 *nal of Geophysical Research: Space Physics*, *98*(A3), 3807-3813. doi:  
 596 [10.1029/92JA02556](https://doi.org/10.1029/92JA02556)
- 597 Borovsky, J. E., & Yakymenko, K. (2017). Substorm occurrence rates, substorm  
 598 recurrence times, and solar wind structure. *Journal of Geophysical Research:*

- 599 *Space Physics*, 122(3), 2973-2998. doi: 10.1002/2016JA023625
- 600 Boscher, D., Bourdarie, S., O'Brien, P., & Guild, T. (2004–2008). *Irbem library v4.*
- 601 3. Retrieved from <https://sourceforge.net/projects/irbem/>
- 602 Burton, R. K., McPherron, R. L., & Russell, C. T. (1975). An empirical relationship
- 603 between interplanetary conditions and Dst. *Journal of Geophysical Research*
- 604 (1896-1977), 80(31), 4204-4214. doi: 10.1029/JA080i031p04204
- 605 Caan, M. N., McPherron, R. L., & Russell, C. T. (1975). Substorm and interplane-
- 606 tary magnetic field effects on the geomagnetic tail lobes. *Journal of Geophys-*
- 607 *ical Research (1896-1977)*, 80(1), 191-194. doi: 10.1029/JA080i001p00191
- 608 Caan, M. N., McPherron, R. L., & Russell, C. T. (1977). Characteristics of
- 609 the association between the interplanetary magnetic field and substorms.
- 610 *Journal of Geophysical Research (1896-1977)*, 82(29), 4837-4842. doi:
- 611 10.1029/JA082i029p04837
- 612 Caan, M. N., McPherron, R. L., & Russell, C. T. (1978). The statistical magnetic
- 613 signature of magnetospheric substorms. *Planetary and Space Science*, 26(3),
- 614 269 - 279. doi: [https://doi.org/10.1016/0032-0633\(78\)90092-2](https://doi.org/10.1016/0032-0633(78)90092-2)
- 615 Cai, X., & Clauer, C. R. (2009). Investigation of the period of sawtooth events.
- 616 *Journal of Geophysical Research: Space Physics*, 114(A6), A06201. doi:
- 617 10.1029/2008JA013764
- 618 Chu, X., McPherron, R. L., Hsu, T.-S., & Angelopoulos, V. (2015). Solar cycle de-
- 619 pendence of substorm occurrence and duration: Implications for onset. *Jour-*
- 620 *nal of Geophysical Research: Space Physics*, 120(4), 2808-2818. doi: 10.1002/
- 621 2015JA021104
- 622 Cowley, S. W. H. (1981). Magnetospheric asymmetries associated with the Y-
- 623 component of the IMF. *Planetary and Space Science*, 29(1), 79 - 96. doi:
- 624 [https://doi.org/10.1016/0032-0633\(81\)90141-0](https://doi.org/10.1016/0032-0633(81)90141-0)
- 625 Dimmock, A. P., Nykyri, K., Osmane, A., & Pulkkinen, T. I. (2016). Statistical
- 626 mapping of ULF Pc3 velocity fluctuations in the Earth's dayside magne-
- 627 tosheat as a function of solar wind conditions. *Advances in Space Research*,
- 628 58(2), 196–207. doi: 10.1016/j.asr.2015.09.039
- 629 Fairfield, D. (1980). A statistical determination of the shape and position of the
- 630 geomagnetic neutral sheet. *Journal of Geophysical Research: Space Physics*,
- 631 85(A2), 775-780. doi: 10.1029/JA085iA02p00775
- 632 Forsyth, C., Rae, I. J., Coxon, J. C., Freeman, M. P., Jackman, C. M., Gjerloev, J.,
- 633 & Fazakerley, A. N. (2015). A new technique for determining Substorm Onsets
- 634 and Phases from Indices of the Electrojet (SOPHIE). *Journal of Geophysical*
- 635 *Research: Space Physics*, 120(12), 10,592-10,606. doi: 10.1002/2015JA021343
- 636 Frey, H. U., & Mende, S. B. (2006). Substorm onsets as observed by IMAGE-FUV.
- 637 In *Proceedings of the 8th international conference on substorms* (pp. 71–76).
- 638 Frey, H. U., Mende, S. B., Angelopoulos, V., & Donovan, E. F. (2004). Substorm
- 639 onset observations by IMAGE-FUV. *Journal of Geophysical Research: Space*
- 640 *Physics*, 109(A10), A10304. doi: 10.1029/2004JA010607
- 641 Friis-Christensen, E., Finlay, C. C., Hesse, M., & Laundal, K. M. (2017). Magnetic
- 642 Field Perturbations from Currents in the Dark Polar Regions During Quiet
- 643 Geomagnetic Conditions. *Space Science Reviews*, 206(1-4), 281-297.
- 644 Friis-Christensen, E., & Wilhjelm, J. (1975). Polar cap currents for different
- 645 directions of the interplanetary magnetic field in the Y-Z plane. *Journal*
- 646 *of Geophysical Research (1896-1977)*, 80(10), 1248-1260. doi: 10.1029/
- 647 JA080i010p01248
- 648 Gjerloev, J. W. (2012). The supermag data processing technique. *Jour-*
- 649 *nal of Geophysical Research: Space Physics*, 117(A9), A09213. doi:
- 650 10.1029/2012JA017683
- 651 Grocott, A., Milan, S. E., Yeoman, T. K., Sato, N., Yukimatu, A. S., & Wild, J. A.
- 652 (2010). Superposed epoch analysis of the ionospheric convection evolution dur-
- 653 ing substorms: IMF BY dependence. *Journal of Geophysical Research: Space*

- 654 *Physics*, 115(A5), A00106. doi: 10.1029/2010JA015728
- 655 Grocott, A., Wild, J. A., Milan, S. E., & Yeoman, T. K. (2009). Superposed  
656 epoch analysis of the ionospheric convection evolution during substorms:  
657 onset latitude dependence. *Annales Geophysicae*, 27(2), 591–600. doi:  
658 10.5194/angeo-27-591-2009
- 659 Holappa, L., Asikainen, T., & Mursula, K. (2020). Explicit IMF dependence in geo-  
660 magnetic activity: Modulation of precipitating electrons. *Geophysical Research*  
661 *Letters*, 47(4), e2019GL086676. doi: 10.1029/2019GL086676
- 662 Holappa, L., & Mursula, K. (2018). Explicit IMF By dependence in high-latitude  
663 geomagnetic activity. *Journal of Geophysical Research: Space Physics*, 123(6),  
664 4728–4740. doi: 10.1029/2018JA025517
- 665 Hsu, T.-S., & McPherron, R. L. (2012). A statistical analysis of substorm associated  
666 tail activity. *Advances in Space Research*, 50(10), 1317 - 1343. doi: 10.1016/j  
667 .asr.2012.06.034
- 668 Huang, C.-S., Reeves, G. D., Borovsky, J. E., Skoug, R. M., Pu, Z. Y., & Le, G.  
669 (2003). Periodic magnetospheric substorms and their relationship with solar  
670 wind variations. *Journal of Geophysical Research: Space Physics*, 108(A6),  
671 1255. doi: 10.1029/2002JA009704
- 672 Kamide, Y., & McIlwain, C. E. (1974). The onset time of magnetospheric  
673 substorms determined from ground and synchronous satellite records.  
674 *Journal of Geophysical Research (1896-1977)*, 79(31), 4787–4790. doi:  
675 10.1029/JA079i031p04787
- 676 Kamide, Y., Perreault, P. D., Akasofu, S. I., & Winningham, J. D. (1977). Depen-  
677 dence of substorm occurrence probability on the interplanetary magnetic field  
678 and on the size of the auroral oval. *Journal of Geophysical Research*, 82(35),  
679 5521–5528. doi: 10.1029/JA082i035p05521
- 680 Kepko, L., McPherron, R. L., Amm, O., Apatenkov, S., Baumjohann, W., Birn, J.,  
681 ... Sergeev, V. (2015). Substorm current wedge revisited. *Space Science*  
682 *Reviews*, 190(1-4), 1–46.
- 683 King, J. H., & Papitashvili, N. E. (2005). Solar wind spatial scales in and compar-  
684 isons of hourly wind and ace plasma and magnetic field data. *Jour-  
685 nal of Geophysical Research: Space Physics*, 110(A2), A02104. doi:  
686 10.1029/2004JA010649
- 687 Koga, D., Gonzalez, W. D., Souza, V. M., Cardoso, F. R., Wang, C., & Liu, Z. K.  
688 (2019). Dayside Magnetopause Reconnection: Its Dependence on Solar Wind  
689 and Magnetosheath Conditions. *Journal of Geophysical Research: Space*  
690 *Physics*, 124(11), 8778–8787. doi: 10.1029/2019JA026889
- 691 Laundal, K. M., Finlay, C. C., Olsen, N., & Reistad, J. P. (2018). Solar wind and  
692 seasonal influence on ionospheric currents from Swarm and CHAMP measure-  
693 ments. *Journal of Geophysical Research: Space Physics*, 123(5), 4402–4429.  
694 doi: 10.1029/2018JA025387
- 695 Laundal, K. M., Gjerloev, J. W., Østgaard, N., Reistad, J. P., Haaland, S., Snekvik,  
696 K., ... Milan, S. E. (2016). The impact of sunlight on high-latitude equivalent  
697 currents. *Journal of Geophysical Research: Space Physics*, 121(3), 2715–2726.  
698 doi: 10.1002/2015JA022236
- 699 Laundal, K. M., & Richmond, A. D. (2017). Magnetic coordinate systems. *Space*  
700 *Science Reviews*, 206, 27–59. doi: 10.1007/s11214-016-0275-y
- 701 Li, H., Wang, C., & Peng, Z. (2013). Solar wind impacts on growth phase dura-  
702 tion and substorm intensity: A statistical approach. *Journal of Geophysical*  
703 *Research: Space Physics*, 118(7), 4270–4278. doi: 10.1002/jgra.50399
- 704 Liou, K. (2010). Polar Ultraviolet Imager observation of auroral breakup. *Jour-  
705 nal of Geophysical Research: Space Physics*, 115(A12), A12219. doi: 10.1029/  
706 2010JA015578
- 707 Liou, K., & Newell, P. T. (2010). On the azimuthal location of auroral breakup:  
708 Hemispheric asymmetry. *Geophysical Research Letters*, 37(23), L23103. doi: 10

- 709 .1029/2010GL045537  
 710 Liou, K., Sotirelis, T., & Mitchell, E. (2020). Control of the east-west compo-  
 711 nent of the interplanetary magnetic field on the occurrence of magnetic  
 712 substorms. *Geophysical Research Letters*, *47*(5), e2020GL087406. doi:  
 713 10.1029/2020GL087406
- 714 Liou, K., Sotirelis, T., & Richardson, I. (2018). Substorm occurrence and intensity  
 715 associated with three types of solar wind structure. *Journal of Geophysical Re-  
 716 search: Space Physics*, *123*(1), 485-496. doi: 10.1002/2017JA024451
- 717 McPherron, R. L. (1970). Growth phase of magnetospheric substorms. *Journal of  
 718 Geophysical Research*, *75*(28), 5592-5599. doi: 10.1029/JA075i028p05592
- 719 McPherron, R. L., & Chu, X. (2018). The midlatitude positive bay index and the  
 720 statistics of substorm occurrence. *Journal of Geophysical Research: Space  
 721 Physics*, *123*(4), 2831-2850. doi: 10.1002/2017JA024766
- 722 McPherron, R. L., Hsu, T.-S., & Chu, X. (2015). An optimum solar wind coupling  
 723 function for the AL index. *Journal of Geophysical Research: Space Physics*,  
 724 *120*(4), 2494-2515. doi: 10.1002/2014JA020619
- 725 McPherron, R. L., Russell, C. T., & Aubry, M. P. (1973). Satellite studies of  
 726 magnetospheric substorms on August 15, 1968: 9. Phenomenological model  
 727 for substorms. *Journal of Geophysical Research*, *78*(16), 3131-3149. doi:  
 728 10.1029/JA078i016p03131
- 729 Milan, S. E., Gosling, J. S., & Hubert, B. (2012). Relationship between interplan-  
 730 etary parameters and the magnetopause reconnection rate quantified from  
 731 observations of the expanding polar cap. *Journal of Geophysical Research:  
 732 Space Physics*, *117*(A3), A03226. doi: 10.1029/2011JA017082
- 733 Milan, S. E., Walach, M.-T., Carter, J. A., Sangha, H., & Anderson, B. J. (2019).  
 734 Substorm onset latitude and the steadiness of magnetospheric convection.  
 735 *Journal of Geophysical Research: Space Physics*, *124*(3), 1738-1752. doi:  
 736 10.1029/2018JA025969
- 737 Morley, S. K., Koller, J., Welling, D. T., Larsen, B. A., Henderson, M. G., & Niehof,  
 738 J. T. (2011). Spacepy - A Python-based library of tools for the space sciences.  
 739 In *Proceedings of the 9th Python in science conference (SciPy 2010)*. Austin,  
 740 TX.
- 741 Newell, P. T., & Gjerloev, J. W. (2011a). Evaluation of SuperMAG auroral electro-  
 742 jet indices as indicators of substorms and auroral power. *Journal of Geophysi-  
 743 cal Research: Space Physics*, *116*(A12), A12211. doi: 10.1029/2011JA016779
- 744 Newell, P. T., & Gjerloev, J. W. (2011b). Substorm and magnetosphere char-  
 745 acteristic scales inferred from the SuperMAG auroral electrojet indices.  
 746 *Journal of Geophysical Research: Space Physics*, *116*(A12), A12232. doi:  
 747 10.1029/2011JA016936
- 748 Newell, P. T., Gjerloev, J. W., & Mitchell, E. J. (2013). Space climate implications  
 749 from substorm frequency. *Journal of Geophysical Research: Space Physics*,  
 750 *118*(10), 6254-6265. doi: 10.1002/jgra.50597
- 751 Newell, P. T., Liou, K., Gjerloev, J. W., Sotirelis, T., Wing, S., & Mitchell, E. J.  
 752 (2016). Substorm probabilities are best predicted from solar wind speed.  
 753 *Journal of Atmospheric and Solar-Terrestrial Physics*, *146*, 28 - 37. doi:  
 754 <https://doi.org/10.1016/j.jastp.2016.04.019>
- 755 Newell, P. T., Sotirelis, T., Liou, K., Meng, C.-I., & Rich, F. J. (2007). A nearly  
 756 universal solar wind-magnetosphere coupling function inferred from 10 mag-  
 757 netospheric state variables. *Journal of Geophysical Research: Space Physics*,  
 758 *112*(A1), A01206. doi: 10.1029/2006JA012015
- 759 Nosé, M., Iyemori, T., Wang, L., Hitchman, A., Matzka, J., Feller, M., ... Çelik,  
 760 C. (2012). Wp index: A new substorm index derived from high-resolution  
 761 geomagnetic field data at low latitude. *Space Weather*, *10*(8), S08002. doi:  
 762 10.1029/2012SW000785
- 763 Nosé, M., Iyemori, T., Sugiura, M., & Slavin, J. A. (1995). A strong dawn/dusk

- 764 asymmetry in Pc5 pulsation occurrence observed by the DE-1 satellite. *Geo-*  
765 *physical Research Letters*, *22*(15), 2053-2056. doi: 10.1029/95GL01794
- 766 Nykyri, K., Ma, X., Dimmock, A., Foullon, C., Otto, A., & Osmane, A. (2017).  
767 Influence of velocity fluctuations on the Kelvin-Helmholtz instability and its  
768 associated mass transport. *Journal of Geophysical Research: Space Physics*,  
769 *122*(9), 9489–9512. doi: 10.1002/2017JA024374
- 770 Paschmann, G., Papamastorakis, I., Baumjohann, W., Sckopke, N., Carlson, C. W.,  
771 Sonnerup, B. U. Ö., & Lühr, H. (1986). The magnetopause for large magnetic  
772 shear: AMPTE/IRM observations. *Journal of Geophysical Research*, *91*(A10),  
773 11099. doi: 10.1029/ja091ia10p11099
- 774 Perreault, P., & Akasofu, S.-I. (1978). A study of geomagnetic storms. *Geophysical*  
775 *Journal of the Royal Astronomical Society*, *54*(3), 547-573. doi: 10.1111/j.1365  
776 -246X.1978.tb05494.x
- 777 Prichard, D., Borovsky, J. E., Lemons, P. M., & Price, C. P. (1996). Time de-  
778 pendence of substorm recurrence: An information-theoretic analysis. *Jour-*  
779 *nal of Geophysical Research: Space Physics*, *101*(A7), 15359-15369. doi:  
780 10.1029/95JA03419
- 781 Reistad, J. P., Laundal, K. M., Ohma, A., Moretto, T., & Milan, S. E. (2020). An  
782 explicit IMF  $b_y$  dependence on solar wind-magnetosphere coupling. *Geophysi-*  
783 *cal Research Letters*, *47*(1), e2019GL086062. doi: 10.1029/2019GL086062
- 784 Russell, C. T., & Brody, K. I. (1967). Some remarks on the position and shape of  
785 the neutral sheet. *Journal of Geophysical Research (1896-1977)*, *72*(23), 6104-  
786 6106. doi: 10.1029/JZ072i023p06104
- 787 Russell, C. T., & McPherron, R. L. (1973). Semiannual variation of geomagnetic ac-  
788 tivity. *Journal of Geophysical Research (1896-1977)*, *78*(1), 92-108. doi: 10  
789 .1029/JA078i001p00092
- 790 Sergeev, V. A., Pellinen, R. J., & Pulkkinen, T. I. (1996). Steady magnetospheric  
791 convection: A review of recent results. *Space Science Reviews*, *75*(3-4), 551–  
792 604.
- 793 Sonnerup, B. U. Ö. (1974). Magnetopause reconnection rate. *Journal of Geophysical*  
794 *Research*, *79*(10), 1546-1549. doi: 10.1029/JA079i010p01546
- 795 Takahashi, K., & Liou, K. (2004). Longitudinal structure of low-latitude Pi2 pul-  
796 sations and its dependence on aurora. *Journal of Geophysical Research: Space*  
797 *Physics*, *109*(A12), A12206. doi: 10.1029/2004JA010580
- 798 Takahashi, K., Liou, K., & Yumoto, K. (2002). Correlative study of ultraviolet au-  
799 rora and low-latitude pi2 pulsations. *Journal of Geophysical Research: Space*  
800 *Physics*, *107*(A12), 1417. doi: 10.1029/2002JA009455
- 801 Tanskanen, E. I. (2009). A comprehensive high-throughput analysis of substorms  
802 observed by IMAGE magnetometer network: Years 1993–2003 examined. *Jour-*  
803 *nal of Geophysical Research: Space Physics*, *114*(A5), A05204. doi: 10.1029/  
804 2008JA013682
- 805 Tenfjord, P., & Østgaard, N. (2013). Energy transfer and flow in the solar wind-  
806 magnetosphere-ionosphere system: A new coupling function. *Journal of Geo-*  
807 *physical Research: Space Physics*, *118*(9), 5659-5672. doi: 10.1002/jgra.50545
- 808 Tsyganenko, N. A., & Fairfield, D. H. (2004). Global shape of the magnetotail cur-  
809 rent sheet as derived from Geotail and Polar data. *Journal of Geophysical Re-*  
810 *search: Space Physics*, *109*(A3), A03218. doi: 10.1029/2003JA010062
- 811 Vasyliunas, V. M., Kan, J. R., Siscoe, G. L., & Akasofu, S.-I. (1982). Scaling rela-  
812 tions governing magnetospheric energy transfer. *Planetary and Space Science*,  
813 *30*(4), 359 - 365. doi: 10.1016/0032-0633(82)90041-1
- 814 Walsh, A. P., Haaland, S., Forsyth, C., Keese, A. M., Kissinger, J., Li, K., ...  
815 Taylor, M. G. (2014). Dawn-dusk asymmetries in the coupled solar wind-  
816 magnetosphere-ionosphere system: A review. *Annales Geophysicae*, *32*(7),  
817 705–737. doi: 10.5194/angeo-32-705-2014
- 818 Weygand, J. M., McPherron, R., Kauristie, K., Frey, H., & Hsu, T.-S. (2008). Re-

- 819           lation of auroral substorm onset to local al index and dispersionless particle  
820           injections. *Journal of Atmospheric and Solar-Terrestrial Physics*, 70(18), 2336  
821           - 2345. doi: <https://doi.org/10.1016/j.jastp.2008.09.030>  
822           World Data Center for Geomagnetism, Kyoto, & Nosé, M. (2016). *Geomagnetic Wp*  
823           *index*. doi: 10.17593/13437-46800  
824           Yeoman, T. K., Freeman, M. P., Reeves, G. D., Lester, M., & Orr, D. (1994). A  
825           comparison of midlatitude Pi 2 pulsations and geostationary orbit particle  
826           injections as substorm indicators. *Journal of Geophysical Research: Space*  
827           *Physics*, 99(A3), 4085-4093. doi: 10.1029/93JA03233